Lab on a Chip

PAPER

View Article Online
View Journal | View Issue



Cite this: *Lab Chip*, 2019, **19**, 1783

# Condensing-enriched magnetic photonic barcodes on superhydrophobic surface for ultrasensitive multiple detection†

Lijun Cai, Feika Bian, Lingyu Sun, Huan Wang and Yuanjin Zhao *

The ultrasensitive detection of multiple nucleic acids has great significance in a broad range of medical fields since nucleic acid samples are usually of small volumes and highly diluted. Herein, we present a novel magnetic photonic crystal (PhC) barcode-integrated condensing-enriched superhydrophobic platform for the ultrasensitive multiple miRNA detection. Droplets containing targets could suck the hydrogel PhC barcodes without losing their targets due to the difference in wettability between the hydrophilic PhC barcodes and hydrophobic substrate. During the evaporation of water from the droplet microreactors, these targets could be effectively enriched in the barcodes for achieving higher sensitivities. As the encoding signals of the PhC barcodes are the characteristic reflection peaks generated by their ordered physical nanostructures, the barcodes are stable and free from any fluorescent background and photobleaching; thus, they are accurate for distinguishing different targets. In addition, with the integration of magnetic nanoparticles into the hydrogel PhC barcodes, they could be imparted with the features of immobilization during change of medium and flexible movement for controlling the reaction, both of which could facilitate the detection processes. Based on this platform, we have demonstrated that the detection limit of multiple miRNAs is improved by about three orders. Thus, our platform is an ideal alternative for the ultrasensitive simultaneous multiplex analysis in medical fields.

Received 4th March 2019,
Accepted 11th April 2019

DOI: 10.1039/c9lc00223e

rsc.li/loc



## Introduction

The ultrasensitive detection of nucleic acids is of enormous significance in the fields of clinical diagnostics, drug development, mutation analysis, and gene therapy.[1–6] Up to now, there have been different signal amplification technologies to realize this goal of detection, including polymerase chain reaction, rolling circle amplification, strand displacement amplification, and hybridization chain reaction.[7–10] However, considering that the nucleic acid samples are of small volumes and highly diluted, the enrichment of the sample solution indeed remains a challenge. Thus, the enrichment of targets from highly diluted solutions to the sensitive area becomes a promising method to raise the concentration in the sensitive area, to obtain a stronger signal and lower the limit of detection.[11–13] Among the various enrichment strategies, the strategy inspired by the Stenocara beetle with a hydrophilic–hydrophobic micropattern on the back for collecting water in the fog provides a simple and effective way to condense and enrich targets from highly diluted solutions to the hydrophilic sensitive area by a wettability difference,[14–18] which effectively increases the detection sensitivity of the different targets.[19–21] Although with the obvious advantages in sensitivity improvement, most of the sensitive areas of the wettability substrates are settled at a fixed point on the superhydrophobic surfaces, which is not flexible enough for the background washing and subsequent detection. In addition, these nucleic-acid sensing platforms cannot meet the requirement of the simultaneous multiplex analysis since they can only carry out a single target test. This greatly limits their practical applications as the single target test is usually not sufficient to guide diagnosis. Therefore, a new wettability enrichment platform that can sensitively, simultaneously and flexibly detect multiplex nucleic acids is still anticipated.

Herein, we present a novel condensing-enriched magnetic photonic crystal (PhC) barcode-integrated superhydrophobic surface for ultrasensitive multiple detection, as illustrated in Fig. 1a. Up to now, barcodes have come to the forefront as a successful tool to realize simultaneous multiplex analysis.[22–25] Various elements of the barcodes, including semiconductor quantum dots, fluorescent particles, or PhC particles, have been developed.[26–28] Among the different barcodes, PhC barcodes have distinct advantages of

*State Key Laboratory of Bioelectronics, School of Biological Science and Medical Engineering, Southeast University, Nanjing 210096, China.*
*E-mail: yjzhao@seu.edu.cn*

† Electronic supplementary information (ESI) available. See DOI: 10.1039/c9lc00223e

remarkable encoding stability, freedom from any fluorescent background and photobleaching since their encoding optical signals are the characteristic reflection peaks generated by the photonic band which depends on the physical structure of its long-range ordered arrangement.[29–35] The properties of the PhC barcodes make them widely applied in multiplex analysis. However, the PhC barcodes, as well as the other kinds of barcodes, have never been integrated to condensing-enriched platforms for improving their sensitivity.

Thus, we, herein, integrated hydrogel PhC barcodes onto a superhydrophobic surface for the ultrasensitive multiple detection. Droplets containing targets could suck the hydrogel PhC barcodes without losing their targets due to the difference in wettability between the hydrophilic PhC barcodes and the hydrophobic substrate. Upon evaporation, these targets are effectively enriched in the barcodes for achieving higher sensitivities. In addition, as magnetic nanoparticles could be incorporated easily into the hydrogel during the generation of the barcodes, the hydrogel PhC barcodes could be imparted with magnetism to enable their immobilization during medium change and their flexible movement for controlling the reaction (Fig. 1b). Based on this platform, we demonstrated that the detection limit of multiple miRNAs is lowered by more than three orders for practical applications. Thus, we believe that our new platform might hold great potential in clinical diagnostics, drug development, and so on.

## Results and discussion

In a typical experiment, silica colloidal crystal beads (SCCBs) with brilliant structural colors and reflection spectra (Fig. 2a–c) were employed as the templates to fabricate the inverse opal-structured hydrogel barcodes. The SCCB templates were prepared by the ordered self-assembly of silica nanoparticles in microfluidic droplets. Scanning electron microscopy (SEM)

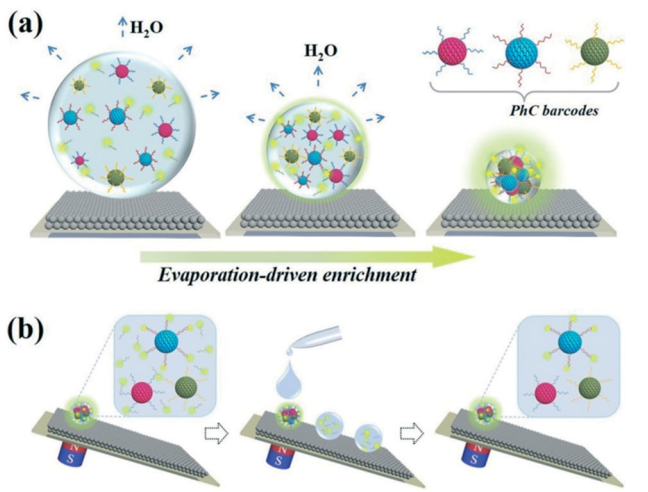


Fig. 1 (a) Illustration of the condensing-enriched process based on the hydrophilic PEG-DA hydrogel PhC barcodes integrated on a superhydrophobic substrate. (b) Illustration of the washing process with magnetic PEG-DA hydrogel PhC barcodes.

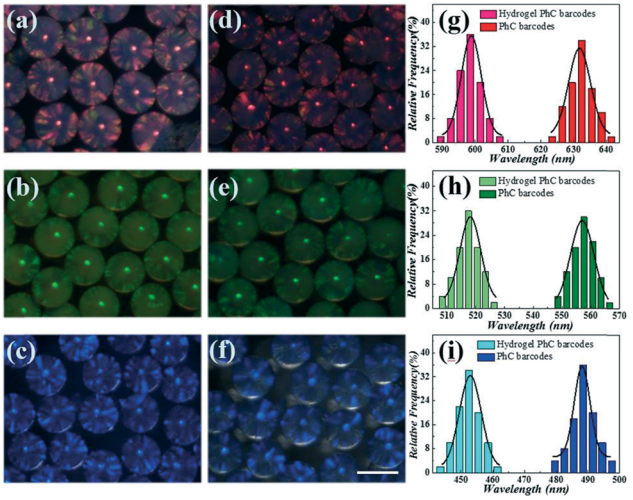


Fig. 2 (a–c) Reflection images of three kinds of PhC barcodes. (d–f) Reflection images of three kinds of inverse opal PEG-DA hydrogel PhC barcodes. (g–i) Reflection spectra comparison of these three kinds of PhC barcodes and their corresponding PEG-DA hydrogel PhC barcodes. Scale bar is 200 μm.

was employed to characterize the microstructures of the SCCB templates. As shown in Fig. S1a,† the SCCBs formed a hexagonal alignment after close packing during the dehydration process. To generate the inverse opal-structured hydrogel barcodes, the SCCB templates were immersed in a pre-gel solution with poly(ethylene glycol) diacrylate (PEG-DA) and acrylic acid (AA). Owing to the capillary force, the pre-gel solution could enter and fill all the interconnected nanopores between the ordered self-assembly silica nanoparticles (Fig. S1b†). After that, ultraviolet (UV) light was utilized to polymerize the pre-gel solution and the SCCB templates were etched by hydrofluoric acid (HF) to obtain the desired inverse opal hydrogel barcodes. As the inverse opal hydrogel barcodes were replicated from the SCCBs templates, they had a similar highly ordered three dimensional inverse opal structure (Fig. S1c†). Thus, the hydrogel barcodes were imparted with a photonic band gap property and showed the corresponding structural color and characteristic reflection peak (Fig. 2d–f). Under normal incidence, the peak positions, $\lambda$, of the barcodes can be estimated by Bragg's equation,

$$\lambda = 1.633 d n_{\text{average}}$$

where $d$ is the center-to-center distance between two neighboring nanopores, and $n_{\text{average}}$ is the average refractive index of the barcodes. Since the duty ratio and gel concentration of different barcodes are the same, the reflective peak positions are mainly decided by the diameter of the silica nanoparticles of the SCCB templates. Therefore, a series of hydrogel barcodes with different sizes of nanopores and reflection peaks can be obtained by using templates assembled with different sizes of silicon dioxide nanoparticles which could be employed to code targets in simultaneous multiplex analysis. As shown in Fig. 2g–i, the statistical results of the

 

reflection peak indicated that the reflection peak location of the SCCB templates we made by using silicon dioxide nanoparticles with sizes around 287 nm, 254 nm and 222 nm was concentrated around 632 nm ± 10 nm, 558 nm ± 10 nm and 488 nm ± 10 nm, respectively. The reflection peaks of the inverse opal hydrogel barcodes derived from these SCCBs were blue shifted by about 30 nm due to the change in their average refractive index ($n_{average}$). As their reflection peak distribution was still relatively concentrated, the hydrogel barcodes could be used as stable encoding microcarriers. The barcodes were stable and free from any fluorescent background and photobleaching. In addition, since there was no dye or other material associated with the code, it was not necessary to be concerned about the chemical instability and fluorescent background during target capture and detection.[36–38]

To carry out the condensing-enriched detection by using the hydrophilic PEG-DA hydrogel PhC barcodes, a hydrophobic substrate was needed. According to the Marangoni effect, higher contact angles lead to a better convective mixing; therefore, a superhydrophobic substrate was better. Considering that the rough surface could reduce the surface energy of the glass slides and the contact area between the water drop and substrate, the colloidal crystal films assembled with silica particles were employed as the basis of the superhydrophobic substrate, which would finally increase the contact angle. As the roughness of the colloidal crystal films were determined by the diameter of the assembled units, different silica particles with diameters of 250 nm, 4 μm and 10 μm, respectively, were employed to assemble the films. To enhance the close-packed junction structures of the silica particles, the glass slides with the colloidal crystal films were sintered at 600 °C, as shown in Fig. S2a.† Subsequently, the colloidal crystal films were immersed in fluorosilane solution to form a strong hydrophobic group containing trifluoromethyl (–CF3) on the surface of the film. The contact angles (CA) of these three kinds of films assembled using 250 nm, 4 μm and 10 μm silica particles were 128°, 138° and 151°, respectively (Fig. S2b–d†). Thus, the colloidal crystal film with arrays assembled with 10 μm silica particles was chosen as the basis of our superhydrophobic substrate.

To investigate the analytical performance and application potential of our platform, miRNAs were employed as the example detection targets. The miRNAs have been proved to repress the expression of important cancer-related genes and might be useful in the diagnosis and treatment of cancer. Different barcodes were chemically modified with the corresponding probes, respectively, for capturing the target miRNA. As the spherical surface of the particles had an ordered porous nanostructure, the barcodes provided a nanopatterned platform for the immobilization of the different probes to realize the highly efficient entrapping of the targets. To demonstrate the enrichment efficiency of our superhydrophobic substrate, the droplets containing the target miRNA and carboxyfluorescein (FAM)-decorated label were drop-cast onto the PEG hydrogel PhC barcodes on the hydrophilic substrate and superhydrophobic substrate, respectively. The droplets evaporated at an environmental condition of 25 °C and 40% relative humidity, and the enrichment process of miRNAs from the highly diluted solution was recorded by a digital camera. Fig. 3a and b shows that the contact line of the droplet on the hydrophilic substrate maintained a contact line till the contact angle was almost 0°, while the contact line of the droplet on the hydrophobic substrate receded with evaporation and the contact angle remained constant as the droplet became smaller. Compared to that on the hydrophobic substrate, the contact area on the hydrophilic substrate was larger, which meant that the targets weren't enriched efficiently. Because of the small interface between the superhydrohobic substrate and the droplet, the analyst droplet did not spread out and thus was concentrated on the hydrophilic area after evaporation. The wettability difference between the hydrogel PhC barcodes and the superhydrophobic substrate drove the droplets containing the targets to be pinned to the hydrogel PhC barcodes without losing their targets upon evaporation, which means that our platform could naturally drive and concentrate targets towards the exact sensitive area. The fluorescence intensity of the hydrogel PhC barcodes that capture targets on the hydrophilic and hydrophobic substrate was measured, and is shown in Fig. 3c and d. The wavelength of the excitation light we used was 488 nm, and the fluorescence spectrum of the FAM label molecule was 520 nm. It was found that the

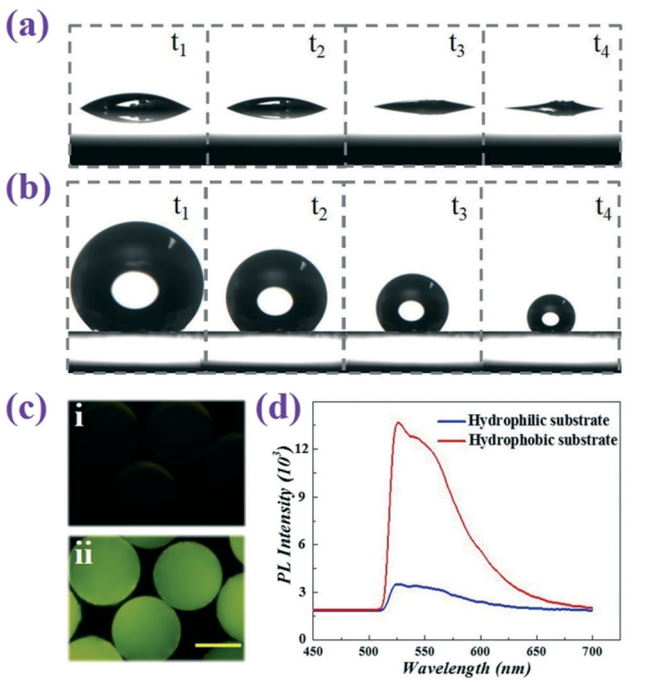


Fig. 3 (a and b) Contact angle images during the enrichment process of the target solution on a hydrophilic substrate (a) and on a superhydrophobic substrate (b). (c and d) The fluorescent image (c) and the measured fluorescence intensity (d) of the barcodes integrated on the hydrophilic substrate (i) and on the hydrophobic substrate (ii), scale bar is 200 μm.

barcodes evaporating on a superhydrophobic substrate had a fluorescence intensity six times higher than that on the hydrophilic substrate. This indicated that the hydrophobic substrate, in contrast to a hydrophilic substrate, benefited the barcodes to obtain stronger signals after the evaporation and enrichment of the target solution.

To realize a better facilitation of the detection processes, the inverse opal PEG hydrogel barcodes were imparted with the ability of controllable movement under magnetic fields by adding magnetic nanoparticles into the pregel solution. The magnetic nanoparticles filled the voids of the SCCBs and endowed the barcodes with magnetism. As shown in Fig. 4a, the barcodes could be attracted to the side of the container by a magnet. When applied to our platform, the magnetism enabled the flexible movement of the hydrogel barcodes for controlling the reaction and their immobilization during background washing (Fig. 4b). The change in fluorescence intensity while washing was recorded and analyzed, as shown in Fig. 4c. It was found that the fluorescence intensity of the barcodes reached constant values with three times of washing, which meant that effective washing was needed after incubation for accurate results. These results indicated that the magnetism of the barcodes enabled the flexible operation, which could facilitate the detection processes.

To further verify the specificity and sensitivity of our integrated platform for microRNA detection in the enrichment process, fluorescence signals were quantitatively analyzed. MiRNA-21, miRNA-205 and miRNA-115 have been found to exhibit abnormal expression in the nonsmall-cell lung cancer (NSCLC) samples. The miRNA sequences used in this study are shown in Table S1.† The probes were chemically anchored into the hydrogel photonic barcodes. Then, the droplet (4 μL) containing 2 μL target miRNA with different concentrations and 2 μL FAM-decorated label with a constant concentration of $10^{-6}$ mol $L^{-1}$ was drop-cast onto the hydrogel PhC barcodes on the superhydrophobic substrate. The ordered porous nanostructure of the barcodes enabled the barcodes to absorb the solution by capillarity like a sponge because of the micropores, which was beneficial for the reaction and the enrichment. Because of the specific recognition of the nucleic acids, the target and label were captured to form a sandwich structure. During the recognition process, the miRNA droplet concentrated at the hydrogel PhC barcodes upon evaporation. Furthermore, due to the Marangoni effect, the nonuniform evaporation rate across the surface of the droplet containing the targets caused a radial flow inside it, which could greatly promote the capture of the targets. The fluorescence intensity of the barcodes was an indirect manifestation of the number of target miRNAs. After the incubation, PBS was employed to wash away the redundant label. The fluorescence intensity of the final barcodes was measured and each point was averaged from at least six independent measurements. As shown in Fig. 5, at concentrations from $10^{-14}$ mol $L^{-1}$ to $10^{-8}$ mol $L^{-1}$, the fluorescence intensity increased exponentially with the concentration of the three kinds of miRNAs. The corresponding calibration plot of the fluorescence intensities *versus* the logarithm of the miRNA concentrations was linear (Fig. 5b). The regression equation for the miRNA detection by our platform was $I = 2055.4 \lg[c] + 30.5$, with a correlation coefficient of 0.9914. The detection limit of the platform was about $5.3 \times 10^{-15}$ mol $L^{-1}$. Compared with the traditional fluorescence chips, the detection limit was lowered by more than three orders, thanks to the enrichment. It demonstrated that the platform could efficiently enrich the analyst from the highly diluted solution droplet, reaching a lower limit of detection. The specificity of the platform was also investigated by testing a sample solution containing a non-complementary miRNA. The histogram of the fluorescence intensity of the barcodes in the presence of the non-

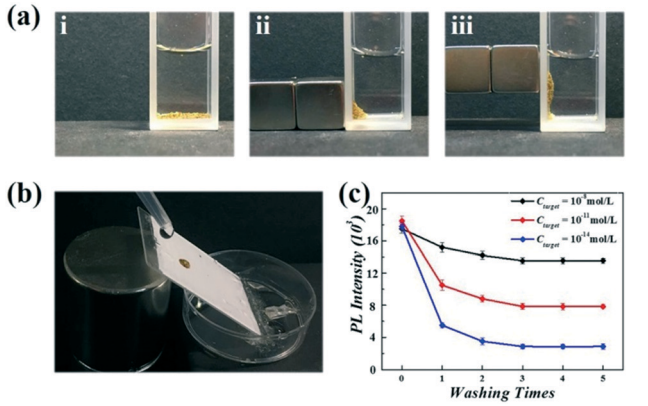


Fig. 4 (a) The movement of the magnetic hydrogel PhC barcodes under the control of magnet. (b) Illustration of the washing process with magnetic PEG-DA hydrogel photonic barcodes. (c) The fluorescence intensity change during the washing process. One milliliter of PBS was employed to wash each time.

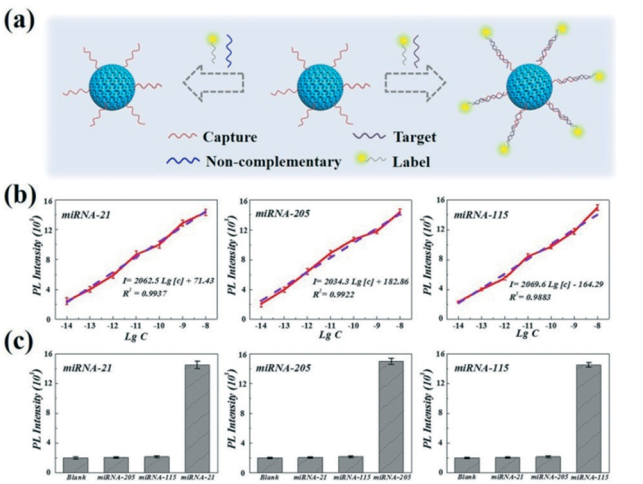


Fig. 5 (a) The schematic of the nucleic acid detection mechanism. (b) Fluorescence intensity at different miRNA concentrations of miRNA-21, miRNA-205 and miRNA-115 ($10^{-14}$ mol $L^{-1}$ to $10^{-8}$ mol $L^{-1}$, 2 μL). (c) Fluorescence intensity of the barcodes modified with the probes of the three kinds of miRNAs after adding the buffer, non-complementary miRNA and target miRNA. The error bars represent the standard deviation from six independent experiments.

complementary miRNA is shown in Fig. 5c. Only the target miRNA endowed an obvious fluorescence signal, which indicated that the system had excellent specificity. Therefore, upon evaporation, our integrated platform could efficiently promote the detection sensitivity with high specificity by condensing the targets from highly diluted solutions to the hydrogel PhC barcodes.

To demonstrate the multiplexed analytical performance of the hydrogel PhC barcodes integrated on the superhydrophobic surface, three kinds of barcodes with characteristic reflection peaks at 488 nm, 558 nm and 632 nm (referred to as blue, green, and red barcodes, respectively) were employed for the simultaneous detection of miRNA-21, miRNA-205 and miRNA-115, respectively. The PEG-DA hydrogel barcodes with different structural colors and reflection spectra were decorated with different corresponding probes, respectively, and then incubated with the mixed solution containing one of the three types of miRNAs and the FAM-decorated label under the same conditions. Fig. 6 shows the microscope images of the mixed barcodes incubated with different targets under bright field and the fluorescence field, respectively. The fluorescence signal indicates the capture of the targets and the reflection peaks are the encoding elements of the barcodes. By combining of the fluorescence signal and the reflection peaks, we could realize the multiple detection and know which target was captured. According to the results, the fluorescence was only observed on the barcodes which could couple with the corresponding miRNA targets. Solutions containing two and three miRNA targets were also detected by our system. Fig. S3† shows that our hydrogel PhC barcodes integrated on the superhydrophobic substrate can realize the detection of more than one target simultaneously.

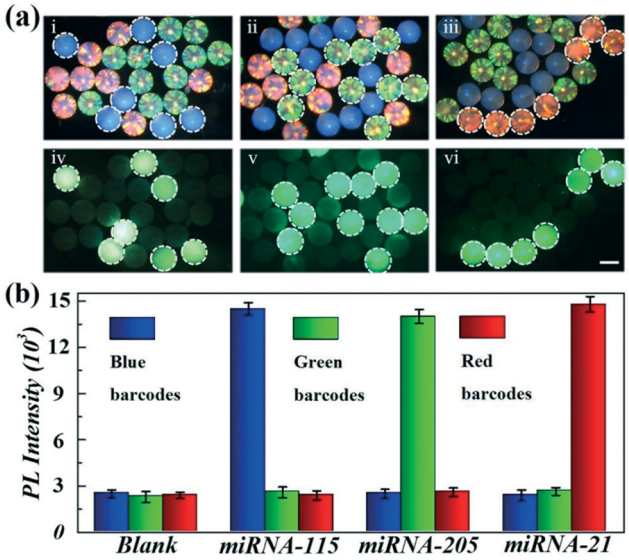


Fig. 6 (a) Optical microscopy images (i–iii) and fluorescence images (iv–vi) of the three kinds of hydrogel PhC barcodes after incubating with the target miRNA; scale bar is 200 μm. (b) The fluorescence statistics after incubating the three different hydrogel PhC barcodes with different targets.

Further fluorescence intensity statistics showed that our platform had good specificity (Fig. 6b). Intense fluorescence could not be observed unless the probe on the barcodes coupled with the target miRNA. Thus, the PEG-DA hydrogel PhC barcodes showed an excellent ability of simultaneous multivariate detection even though the targets were highly diluted for they were integrated on the superhydrophobic substrate.

## Experimental

### Material

FAM-decorated label, miRNA-21, miRNA-205, miRNA-115 and their corresponding probes were purchased from Nanjing Ruizhen Biotechnology Co. LTD. Phosphate buffer saline (PBS, 0.05 M, pH 7.4) was self-prepared. Epoxy chloropropane (ECH) was purchased from Aladdin Industrial Corporation. Acrylic acid, 2-hydroxy-2-methylpropiophenone (HMPP) photoinitiator and Poly(ethylene glycol) diacrylate (PEG-DA) with the molecular weight of 700 were purchased from Sigma-Aldrich, Shanghai, China. All buffers were self-prepared using water purified in a Milli-Q system (Millipore, Bedford, USA). The silica nanoparticles were self-prepared. The magnetic nanoparticles were purchased from Nanjing Nanoeast Biotech Co. LTD.

### Preparation of SCCBs

The SCCBs were generated by the microfluidic droplet device, using the assembly of silica nanoparticles by a method based on our previous work.[39] The syringe pumps and constant pressure pumps were purchased from Longer Precision Pump Co., Ltd. The continuous phase in this protocol was silicone oil (Shinetsu, 50cs, Japan) and the dispersed phase was the monodisperse silica nanoparticle aqueous suspension. The silica nanoparticle aqueous suspension was cut into droplets by silicone oil in the microfluidic droplet device. After that, the droplets were evaporated at 80 °C for 8 h to achieve the colloidal crystal beads. Then, hexane was used to remove the silicone oil on the beads. Finally, the SCCBs were calcined at 800 °C for 12 h in a muffle furnace to stabilize the structure.

**Preparation of the inverse opal hydrogel magnetic barcodes.** The silica colloidal crystal beads fabricated using the microfluidic devices were used as the template to assemble the inverse opal hydrogel PhC barcodes. The SCCB templates were prepared by the ordered self-assembly of silica nanoparticles in microfluidic droplets. Firstly, the dried silica colloidal crystal beads with brilliant structural colors and reflection spectra were immersed in the pregel solution (20% PEG-DA, 10% AA, 5% magnetic nanoparticles solution and 1% HMPP) for 30 minutes. The concentration of the magnetic nanoparticles with a diameter of about 10 nm used here was 4 mg $ml^{-1}$. Ultraviolet light was utilized to polymerize the mixed solution of the pregel solution and SCCBs after the pregel solution had filled the voids. Then, the pregel solution on the surface of the templates was mechanically removed. Finally, the inverse opal-structured hydrogel barcodes were

obtained by etching the silica nanoparticles in the templates with hydrofluoric acid (HF).

**Preparation of the superhydrophobic substrate.** The colloidal crystal film was employed as the basis of the superhydrophobic substrate. Firstly, the colloidal crystal film was obtained by the self-assembly of the silica nanoparticles with a diameter of 10 μm on glass slides. Then, to enhance the close-packed junction structures of the SiO2 nanoparticles, the glass slides with the fabricated colloidal crystal arrays were sintered at 600 °C. Finally, the superhydrophobic substrate was obtained by immersing the colloidal crystal film in a mixed solution (1% 1*H*,1*H*,2*H*,2*H*-perfluorodecyl triethoxysilane, 1% glacial acetic acid and 98% isopropyl alcohol) for 4 h.

**Preparation of the miRNA-conjugated inverse opal hydrogel PhC barcodes.** Three kinds of miRNA probes (miRNA-21, miRNA-205 and miRNA-115) were dissolved in sterile water at a concentration of $10^{-4}$ mol $L^{-1}$. Firstly, the inverse opal hydrogel PhC barcodes prepared earlier were treated with 2-morpholinoethanesulfonic acid (MES), 1-ethyl-3-(3-dimethylamino-propyl)carbodiimide (EDC) and *N*-hydroxysuccinimide (NHS) for 30 min at 37 °C in a constant shaker. Then, the blue inverse opal barcodes were coated with amino-modified miRNA-21, the green barcodes were coated with amino-modified miRNA-205 and the red barcodes were coated with amino-modified miRNA-115 after being washed with PBS for 6 h at 25 °C. Finally, the different functionalized inverse opal barcodes with their own probes were prepared successfully after washing with the buffer solution.

### Capture of miRNAs

For single detection, the pre-prepared blue hydrogel PhC barcodes coated with amino-modified miRNA-21 were placed on the superhydrophobic substrate. Then, a solution with 2 μL of different concentrations of the target miRNA-21 and 2 μL of constant concentration of the FAM-decorated label was drop-cast onto the magnetic hybrid hydrogel photonic barcodes on the superhydrophobic substrate. The concentration of the target miRNA-21 ranged from $10^{-14}$ mol $L^{-1}$ to $10^{-8}$ mol $L^{-1}$, but the FAM-decorated label remained at a constant concentration of $10^{-6}$ mol $L^{-1}$. After 1 hour of incubation, PBS was employed three times to wash away the redundant labeled miRNAs. Finally, the result of the capture was determined by measuring the fluorescence intensity of the hydrogel PhC barcodes under a fluorescence microscope. Each fluorescence intensity statistics was measured six times. For multivariate detection, the pre-prepared three kinds of magnetic barcodes coated with amino-modified miRNA-21, miRNA-205 and miRNA-115 were mixed and placed on the superhydrophobic substrate. Then, the solution with only one target miRNA ($10^{-8}$ mol $L^{-1}$, 2 μL) and the FAM-decorated label ($10^{-6}$ mol $L^{-1}$, 2 μL) was drop-cast on the barcodes for single detection. Experiments with solutions with two and three miRNAs were also carried out. After 1 hour of incubation, PBS was employed to wash away the redundant target and labeled miRNAs. Finally, the result of the multivariate detection was determined by observing the fluorescence images under a microscope.

## Conclusions

In summary, we have developed a condensing-enriched magnetic photonic barcode-integrated superhydrophobic surface for the ultrasensitive multiple miRNA detection. Thanks to the wettability difference, the targets in the highly diluted solution could be condensed to the magnetic PEG-DA hydrogel barcodes and enriched with evaporation, which lowered the limit of detection by more than three orders. The excellent optical properties of the PEG-DA hydrogel PhC barcodes which possess stable characteristic reflection peaks, free from any fluorescent background and photobleaching, enabled the simultaneous multivariate analysis. In addition, the magnetism of the barcodes made it feasible to control the movement of the barcodes which benefited the facilitation of the reaction process. This novel platform provides a simple, highly sensitive, and flexible method for ultrasensitive multiple biological analysis. We hypothesized that it would significantly promote the development of applications in ultrasensitive biological analysis, clinical diagnosis, and related research areas.

## Author contributions

L. Cai and F. Bian contributed equally to this work; Y. Zhao conceived the idea and designed the experiment; L. Cai carried out the experiments; L. Cai, F. Bian and Y. Zhao analyzed the data and wrote the paper; H. Wang and L. Sun contributed to the scientific discussion of the article.

## Conflicts of interest

There are no conflicts to declare.

## Acknowledgements

This work was supported by the National Key Research and Development Program of China (2017YFA0700404), the NSAF Foundation of China (grant U1530260), the Natural Science Foundation of Jiangsu (Grant no. BE2018707), the Scientific Research Foundation of Southeast University, and the Scientific Research Foundation of the Graduate School of Southeast University.

## Notes and references

1 M. Piwecka, P. Glažar, L. R. Hernandez-Miranda, S. Memczak, S. A. Wolf, A. Rybak-Wolf, A. Filipchyk, F. Klironomos, C. A. C. Jara, P. Fenske, T. Trimbuch, T. Zywitza, V. Plass, M. Schreyer, L. Ayoub, S. Kocks, C. Kühn, R. Rosenmund, C. Birchmeier and C. N. Rajewsk, *Science*, 2017, **357**, eaam8526.

 

2 S. Goodwin, J. D. McPherson and W. R. McCombie, *Nat. Rev. Genet.*, 2016, **17**, 333–351.
3 H. Liu, H. Zhang, X. Wu, D. Ma, J. Wu, L. Wang, Y. Jiang, Y. Fei, C. Zhu, T. Rong, P. Jungblut, G. Pei, A. Dorhoi, Q. Yan, F. Zhang, R. Zheng, S. Liu, H. Liang, Z. Liu, H. Yang, J. Chen, P. Wang, T. Tang, W. Peng, Z. Hu, Z. Xu, X. Huang, J. Wang, H. Li, Y. Zhou, F. Liu, D. Yan, S. H. Kaufmann, C. Chen, Z. Mao and B. Ge, *Nature*, 2018, **563**, 131–136.
4 W. Lu, Y. Chen, Z. Liu, W. Tang, Q. Feng, J. Sun and X. Jiang, *ACS Nano*, 2016, **10**, 6685–6692.
5 J. Shi, P. W. Kantoff, R. Wooster and O. C. Farokhzad, *Nat. Rev. Cancer*, 2017, **17**, 20–37.
6 M. W. Shen, M. Arbab, J. Y. Hsu, D. Worstell, S. J. Culbertson, O. Krabbe, C. A. Cassa, D. R. Liu, D. K. Gifford and R. I. Sherwood, *Nature*, 2018, **563**, 646–651.
7 X. Huang, Y. Liu, B. Yung, Y. Xiong and X. Chen, *ACS Nano*, 2017, **11**, 5238–5292.
8 R. A. Goodnow, C. E. Dumelin and A. D. Keefe, *Nat. Rev. Drug Discovery*, 2017, **16**, 131–147.
9 M. Liu, Q. Zhang, D. Chang, J. Gu, J. D. Brennan and Y. A. Li, *Angew. Chem., Int. Ed.*, 2017, **56**, 6142–6146.
10 M. Kühnemund, Q. Wei, E. Darai, Y. Wang, I. Hernández-Neuta, Z. Yang, D. Tseng, A. Ahlford, L. Mathot, T. Sjöblom, A. Ozcan and M. Nilsson, *Nat. Commun.*, 2017, **8**, 13913.
11 S. Yang, X. Dai, B. B. Stogin and T. S. Wong, *Proc. Natl. Acad. Sci. U. S. A.*, 2016, **113**, 268–273.
12 R. Hernandez-Perez, Z. H. Fan and J. L. Garcia-Cordero, *Anal. Chem.*, 2016, **88**, 7312–7317.
13 L. Xu, Y. Chen, G. Yang, W. Shi, B. Dai, G. Li, Y. Cao, Y. Wen, X. Zhang and S. Wang, *Adv. Mater.*, 2015, **27**, 6878–6884.
14 Y. Zhao, C. Yu, H. Lan, M. Cao and L. Jiang, *Adv. Funct. Mater.*, 2017, **27**, 1701466.
15 C. Cheng, Y. Cai, G. Guan, L. Yeo and D. Wang, *Angew. Chem., Int. Ed.*, 2018, **57**, 11177–11181.
16 X. Liu, C. Leng, L. Yu, K. He, L. J. Brown, Z. Chen, J. Cho and D. Wang, *Angew. Chem., Int. Ed.*, 2015, **54**, 4851–4856.
17 J. Ju, X. Yao, X. Hou, Q. Liu, Y. S. Zhang and A. Khademhosseini, *J. Mater. Chem. A*, 2017, **5**, 16273–16280.
18 J. Ju, H. Bai, Y. Zheng, T. Zhao, R. Fang and L. Jiang, *Nat. Commun.*, 2012, **3**, 1247.
19 J. Hou, H. Zhang, Q. Yang, M. Li, L. Jiang and Y. Song, *Small*, 2015, **11**, 2738–2742.
20 H. Li, Q. Yang, J. Hou, Y. Li, M. Li and Y. Song, *Adv. Funct. Mater.*, 2018, **28**, 1800448.
21 J. Hou, H. Zhang, Q. Yang, M. Li, Y. Song and L. Jiang, *Angew. Chem., Int. Ed.*, 2014, **53**, 5791–5795.
22 L. Shang, Y. Cheng and Y. Zhao, *Chem. Rev.*, 2017, **117**, 7964–8040.
23 H. Wang, Z. Zhao, Y. Liu, C. Shao, F. Bian and Y. Zhao, *Sci. Adv.*, 2018, **4**, eaat2816.
24 F. Fu, Z. Chen, Z. Zhao, H. Wang, L. Shang, Z. Gu and Y. Zhao, *Proc. Natl. Acad. Sci. U. S. A.*, 2017, **114**, 5900–5905.
25 M. Qin, Y. Huang, Y. Li, M. Su, B. Chen, H. Sun, P. Yong, C. Ye, F. Li and Y. Song, *Angew. Chem., Int. Ed.*, 2016, **55**, 6911–6914.
26 Y. Xu, H. Wang, C. Luan, F. Fu, B. Chen, H. Liu and Y. Zhao, *Adv. Funct. Mater.*, 2018, **28**, 1704458.
27 Y. Cao, W. Geng, R. Shi, L. Shang, G. I. N. Waterhouse, L. Liu, L. Z. Wu, C. H. Tung, Y. Yin and T. Zhang, *Angew. Chem.*, 2016, **128**, 15176–15181.
28 C. Li, Z. Lu, Q. Zhang, J. Ge, S. Aloni, Z. Shi and Y. Yin, *Sci. China Mater.*, 2015, **58**, 481–489.
29 M. Wang, L. He, W. Xu, X. Wang and Y. Yin, *Angew. Chem., Int. Ed.*, 2015, **54**, 7077–7081.
30 J. S. Lee, C. H. Lim, S. M. Yang and S. H. Kim, *Langmuir*, 2014, **30**, 2369–2375.
31 H. Kang, J. S. Lee, W. S. Chang and S. H. Kim, *Adv. Mater.*, 2015, **27**, 1282–1287.
32 Q. Fu, A. Chen, L. Shi and J. Ge, *Chem. Commun.*, 2015, **51**, 7382–7385.
33 J. Hou, M. Li and Y. Song, *Angew. Chem., Int. Ed.*, 2018, **57**, 2544–2553.
34 K. Zhong, L. Wang, J. Li, S. Van Cleuvenbergen, C. Bartic, K. Song and K. Clays, *Langmuir*, 2017, **33**, 4840–4846.
35 J. Hou, M. Li and Y. Song, *Nano Today*, 2018, **22**, 132–144.
36 M. Li, Q. Liao, J. Zhang, L. Jiang, Y. Song, D. Zhu, D. Chen, F. Tang and X. Wang, *Appl. Phys. Lett.*, 2007, **91**, 203516.
37 M. Li, A. Xia, J. Wang, Y. Song and L. Jiang, *Chem. Phys. Lett.*, 2007, **444**, 287.
38 M. Li, F. He, Q. Liao, J. Liu, X. Liang, L. Jiang, Y. Song, S. Wang and D. Zhu, *Angew. Chem.*, 2008, **120**, 7368–7372.
39 Y. Zhao, X. Zhao, C. Sun, J. Li, R. Zhu and Z. Gu, *Anal. Chem.*, 2008, **80**, 1598–1605.